Cement and Concrete Research 40 (2010) 197–207

Contents lists available at ScienceDirect

Cement and Concrete Research

journal homepage: http://ees.elsevier.com/CEMCON/default.asp

Identification of viscoelastic C-S-H behavior in mature cement paste by FFT-based homogenization method

Vít Šmilauer [a,*], Zdeněk P. Bažant [b]

[a] Department of Mechanics, Faculty of Civil Engineering, Czech Technical University in Prague, Thákurova 7, Prague 6, 166 29, Czech Republic
[b] Department of Civil and Environmental Engineering, Northwestern University, 2145,Sheridan Road, Evanston, Illinois 60208, United States

ARTICLE INFO

Article history:
Received 21 January 2008
Accepted 4 October 2009

Keywords:
Micromechanics (C)
Creep (C)
Cement paste (D)
Microprestress

ABSTRACT

A powerful and robust numerical homogenization method based on fast Fourier transform (FFT) is formulated to identify the viscoelastic behavior of calcium silicate hydrates (C-S-H) in hardened cement paste from its heterogeneous composition. The identification is contingent upon the linearity of the creep law. To characterize cement paste microstructure, the model developed by Bentz at the National Institute of Standards and Technology, which has the resolution of 1 μm, is adopted. Model B3 for concrete creep is adapted to characterize the creep of C-S-H in cement paste. It is found that the adaptation requires increasing the exponent of power law asymptote of creep compliance. This modification means that the rate of attenuation of creep with time is lower in C-S-H than in cement paste, and is explained by differences in stress redistribution. In cement paste, the stress is gradually transferred from the creeping C-S-H to the non-creeping components. The viscoelastic properties of C-S-H at the resolution of 1 μm were identified from creep experiments on cement pastes 2 and 30 years old, having the water–cement ratio of 0.5. The irreversible part of C-S-H creep, obtained from these old specimens at almost saturated state, is found to be negligible unless the specimens undergo drying and resaturation prior to the creep test.

1. Introduction

The existing models for predicting concrete creep are either entirely empirical or are based only on macroscopic mathematical arguments [1]. They do not take into account the random microstructure and its evolution. Thanks to the recent progress in micromechanics, material modeling and numerical simulation, it has now become possible to relate creep to the material properties on the micrometer and nanometer scales. Here we aim at mathematical formulation of this relationship.

It is beyond doubt that the mechanics of composite materials can bring new insight into the creep behavior of concrete. The recent work in linear elastic homogenization of concrete [2] or cement paste [3] demonstrated the potential of analytical or numerical homogenization methods (although, for very young hydrating concrete, these methods might not be sufficiently realistic, due to the simplifying assumption of perfect bonding among all phases, which is poor for early ages [2]). Extension of these methods to basic creep of aging concrete or hardened cement paste is made possible by linearity of the constitutive law, which permits reducing the creep problem to a quasi-static elasticity problem. Simple analytical composite models, distinguishing the creeping and non-creeping constituents, have recently been formulated and shown to give realistic predictions [4–7].

It has long been recognized that creep occurs predominantly in the cement gel of hardened cement paste. Cement gel is a product of chemical binding of capillary water. The gel is formed in the available capillary pores, which are filled with water at the beginning of hydration. In Portland cement paste, the cement gel is a mixture of several chemical phases, among which the C-S-H occupy the most space. Examples of other phases are ettringite, calcium hydroxide and hydrogarnet.

The microstructure of cement paste will be here simulated according to Bentz's cement hydration model CEMHYD3D [8]. Concrete creep model B3 [9–11], updated in [1], will be adapted to the C-S-H phase, and the macroscopic response will be calculated using the numerical homogenization method based on the fast Fourier transform (FFT). The analysis will be here restricted to the creep at no moisture exchange, called the basic creep, and to well-hydrated cement pastes. Modeling of the entire hydration process, including the early aging due to gradual deposition of stress-free C-S-H layers on the pore surfaces in loaded specimens during hydration [12], is beyond the scope of this study, although a future extension of the present model to this general case is possible.

It must be emphasized that the identified properties of C-S-H are obtained at the resolution of 1 μm. Therefore the nanoporosity of C-S-H is included. Although further downscaling to the C-S-H building blocks is possible [13], it will not be explored here.

Can the creep in cement paste originate from chemical phases other than the C-S-H? Not to a significant degree. This is confirmed by

* Corresponding author.
E-mail address: vit.smilauer@fsv.cvut.cz (V. Šmilauer).

0008-8846/$ – see front matter © 2009 Elsevier Ltd. All rights reserved.
doi:10.1016/j.cemconres.2009.10.003

nano-indentation tests of pure cement clinker minerals (C_3S, C_2S, C_3A, and C_4AF), which exhibited no creep at all [14].

Hardened cement paste with water–cement ratio of w/c = 0.5 was indented in a grid pattern in order to extract the short-term creep properties of individual paste phases [15]. The observed magnitude of creep obtained by fitting a logarithmic curve clearly showed bimodal distribution which was aligned with two types of C-S-H only [15]. It was concluded that other solid phases (clinker minerals and portlandite) do not creep and act merely as a restraint in the system. The creep effect of other phases (ettringite and hydrogarnet), if any, would be negligible since their volume fractions are very small.

Is it possible to prepare, on the macroscale level, homogeneous C-S-H which would be identical to the C-S-H in hardened cement paste? Not to the authors' best knowledge. Therefore, the identification of C-S-H properties must follow one of two indirect approaches: (i) short-time nano-indentation tests, several minutes in duration (as limited by measurement stability), on the scale of 100 nm, at which the C-S-H appears rather homogeneous, or (ii) micromechanical inverse analysis of creep data. The latter is pursued here. While nano-indentation is an invaluable tool for accessing the short-time creep behavior of chemical phases, the micromechanical approach can follow a real time simulation of creep experiment without the necessity of extrapolating the C-S-H creep. The objective of this paper is to develop a numerical homogenization procedure for scale bridging of creep behavior of C-S-H from the nano-level to the macro-level of cement paste.

The moisture effects on creep are rather complex [16–18] and are basically of two types: (1) The moisture content effect, which causes that, at thermodynamic equilibrium at constant and uniform pore humidity (relative vapor pressure), creep is an order-of-magnitude lower in a dry state than at saturation; and (2) the transient effect, called drying creep (or Pickett effect), which causes that, during drying, creep strongly increases. The latter effect is twofold: (2a) partly an apparent phenomenon, due to more intense distributed microcracking in companion shrinkage specimens, and (2b) partly a real phenomenon, due to increased mobility of atomic connections across nano-pores caused by migration of water molecules [16,17,19]. Effects (1) and (2b) arise from the movement and fixation of water molecules in the C-S-H nanostructure [20]. Various early theories [18,21,22], such as the seepage (consolidation) theory, interlayer theory, viscous shear theory and thermal activation theory, have been shown to be insufficient or invalid.

2. Constitutive law for C-S-H

The creep of C-S-H, which is believed to be the dominant source of creep in concrete, is elastically restrained by all the non-creeping phases, which include the mineral aggregates in concrete and all the other phases in cement paste consisting of the unhydrated cement grains and calcium hydroxide crystals. Since the hardened cement paste occupies up to 40% of the volume of ordinary concrete, the magnitude of creep of C-S-H is expected to be considerably higher than that observed at the level of concrete or hardened cement paste. As the elastic restraint does not change significantly the time evolution of creep curves, the compliance functions of C-S-H and of concrete are expected to be similar. Therefore we adopt for C-S-H a compliance function of the B3 type [1,9,16,17], which is supported by theoretical arguments and agrees quite well with experiments, including the broad ranges from very short to very long load durations and from very young to very old ages [1,10]. For the case of no moisture or temperature change, the flow term in model B3 can be simplified to a logarithmic law, which will be adopted here. If drying creep is excluded, the B3 compliance function for uniaxial stress has the form

$$J(t,t') = q_1 + C_v(t,t') + q_4 \ln\left(\frac{t}{t'}\right) \tag{1}$$

$$C_v(t,t') = \int_{t'}^{t} v^{-1}(t)\,\dot{C}_g(\tau - t')\,\mathrm{d}\tau = \int_{t'}^{t} v^{-1}(t)\,\frac{n(\tau-t')^{n-1}}{\lambda_0^n + (\tau-t')^n}\,\mathrm{d}\tau \tag{2}$$

$$v^{-1}(t) = \left[q_2\left(\frac{\lambda_0}{t}\right)^m + q_3\right]. \tag{3}$$

Several parameters were found to be constant for concrete, independent of its type and curing conditions: $\lambda_0 \approx 1$ day, $m = 0.5$ and $n = 0.1$ [23].

The creep compliance in Eq. (1) can be related to the C-S-H indentation modulus. C-S-H compliance $J(t' + 3\cdot10^{-5}\,\text{day}, t')$ corresponds to assuming the duration of 2.6 s (or $3\cdot10^{-5}$ day) for the unloading part of the nano-indentation tests, i.e., the part that is used to evaluate the E-modulus on the nanoscale.

If we separate the final constant part of $v(t)$, characterized by parameter q_3 in Eq. (3), and integrate Eq. (2), we obtain $C_v(t,t') = q_3 \ln[1 + \lambda_0^{-n}(t-t')^n]$, which is known as the log-power law [23]. For short times, this law evolves asymptotically as a power function of load duration $t-t'$ and, for long times, it evolves asymptotically as a logarithmic function. Since the time lag $t-t'$ is the only time variable present (i.e., t and t' both do not appear as independent variables), this law exhibits no aging and thus may be regarded as the 'intrinsic' compliance function for the creep of non-aging cement gel.

The cement hydration is a solidification process which causes the volume fraction of cement gel to increase with age. This decreases creep because the applied stress is gradually redistributed to the newly formed cement gel. This effect is captured by function $v(t)$, which may be interpreted as the effective load-bearing fraction of cement gel, where aging is controlled by parameter q_2.

In extension to stress varying in time, the hypothesis of linearity with respect to stress agrees with test data, provided that there is no drying and that the stresses are less than approximately 50% of the strength limit of concrete, which is the range of service stresses in structures. The total strain may thus be calculated according to the principle of superposition, summing the strain histories produced by infinitesimal stress increments $\mathrm{d}\sigma(t')$ [21,22,24]

$$\varepsilon(t) = \int_0^t J(t,t')\,\mathrm{d}\sigma(t') + \varepsilon_0 \tag{4}$$

where ε_0 is the initial strain, which includes shrinkage, thermal strain and cracking strain. For numerical solution, it is convenient to convert Eq. (4) to a rate-type formulation based on Kelvin or Maxwell chain. For the case of Kelvin chain [21,24,25]

$$\dot{\varepsilon}_\mu(t) + \tau_\mu \ddot{\varepsilon}_\mu(t) = \frac{\dot{\sigma}(t)}{E_\mu(t)} \tag{5}$$

where τ_μ are properly chosen retardation times of the μ-th Kelvin unit ($\mu = 1,2\ldots N$), $E_\mu(t)$ are the corresponding moduli, which in general are age-dependent, and $\varepsilon_\mu(t)$ are the strains in the individual Kelvin units.

3. Continuous retardation spectrum for non-aging creep

An arbitrary non-aging creep compliance function $C_g(t-t')$ may be approximated by a chain of N Kelvin units in the form of Dirichlet series [26]. For a suitable selection of N retardation times τ_μ, which should be uniformly spaced over the logarithmic time scale, elastic moduli $E_\mu(t)$ of all Kelvin units can be found by least-square fitting of the compliance function. For age-dependent $E_\mu(t)$, the discrete retardation spectrum (plot of E_μ versus τ_μ) obtained by fitting has two disadvantages—it is not unique, and the E_μ obtained may be negative or decreasing for short periods of time [27]. Although the thermodynamic restrictions are not necessarily violated (because they do not apply to the parameters of internal variables such as

$E_\mu(t)$), their satisfaction is not guaranteed and it is not necessarily justified to attribute to E_μ some physical meaning.

Demonstration of the possibility to account for concrete aging by two, and only two, separate functions—the volume growth function $v(t)$ and the aging viscous flow term [17]—made it simple to introduce a unique continuous retardation spectrum $L(\tau)$ based on Laplace transformation, which corresponds to the limit case of infinitely many Kelvin units with infinitely small moduli E_μ. Widder's order-k asymptotic inversion formula then allows a simple and accurate approximation of arbitrary non-aging creep compliance function such as non-aging log-power law [26]. Aside from simplicity in identifying E_μ, the aforementioned three disadvantages are avoided—the continuous spectrum is unique and all E_μ are guaranteed to be positive. From the continuous spectrum, it is then easy to determine the discretized values of E_μ for a finite Kelvin chain, which are needed for computer analysis. To this end, the retardation time interval, $\Delta(\log\ \tau_\mu)$, separating two adjacent discrete Kelvin units, must be chosen. To get a smooth creep compliance curve, it suffices to use $\Delta(\log\ \tau_\mu) = \log 10 = 1$ [26]. Hence,

$$\frac{1}{E_\mu} = L(\tau_\mu)\ln 10\Delta(\log\tau_\mu). \tag{6}$$

A third-order approximation of $L(\tau_\mu)$ ($k=3$) has been derived for the non-aging log-power law $C_g(t-t')$ [26]. Even though only a limited time range, such as $(10^{-2}, 10^4)$ days, is normally of interest, it is necessary to introduce discrete relaxation times covering the range $(\tau_{\min},\tau_{\max})$ where $\tau_{\max}$ is about the double of the longest creep duration of interest and $\tau_{\min}$ is extremely small, such as 10^{-20} days. The reason why one needs to consider such a short retardation time, far shorter than the shortest time of numerical simulation, is that the E_μ values for such small τ_μ contribute to the overall compliance appreciably. Even though the set of Kelvin units for such short times, shorter than τ_1, behaves elastically, they cannot be replaced by one spring (corresponding to q_1) because each compliance component $1/E_\mu$ that contributes to the elastic compliance $1/E$ undergoes different aging (due to the term associated with q_2).

Consequently, the non-aging compliance function of cement gel is approximated with a constant compliance corresponding to $\tau_{\min},\ldots\tau_0$ and a truncated time-dependent compliance corresponding to $\tau_1,\ldots\tau_{\max}$

$$C_g(t-t') = \sum_{\mu=1}^{\max}\frac{1}{E_\mu}\left(1-e^{-(t-t')/\tau_\mu}\right) \approx \underbrace{\sum_{\mu=\min}^{0}\frac{1}{E_\mu}}_{\text{degenerated as elastic}} + \underbrace{\sum_{\mu=1}^{\max}\frac{1}{E_\mu}\left(1-e^{-(t-t')/\tau_\mu}\right)}_{\text{creeping Kelvin units.}} \tag{7}$$

Note that, if the Maxwell chain model were used, the first relaxation time τ_1 would not need to be so short since relaxed Maxwell units carry no stresses, and would only need to satisfy the condition $\tau_{\min}<\tau_0$. Also, no sum from $\tau_{\min}$ to τ_0 would be needed because these Maxwell units are relaxed to zero stress.

Although the Kelvin chain approach is more mathematically complicated than the Maxwell chain approach, it became well-established. The reason is that the parameters of Kelvin units are easier to identify directly from creep experiments, which are easier to carry out than the relaxation experiments.

The aforementioned simple procedure significantly reduces the number of Kelvin units necessary for creep computations, and consequently the number of internal variables $\gamma_\mu(t)$. For simulations from 10^{-4} day to 100 years, 10 Kelvin units generally suffice. Thanks to the uniqueness and independence of the non-aging cement gel compliance function of the age at loading, the E_μ values need to be computed only once, at the beginning of simulation.

4. Exponential algorithm

Introduction of aging function $v(t)$ and a suitable definition of internal variables $\gamma_\mu(t)$ makes it possible to convert Eq. (5) to the following system of first-order differential equations, identical to those for a non-aging Kelvin chain [23,24]

$$\gamma_\mu(t) = \tau_\mu v(t)\,\dot{\varepsilon}_\mu(t) \tag{8}$$

$$\dot{\gamma}_\mu(t) + \frac{1}{\tau_\mu}\gamma_\mu(t) = \frac{\dot{\sigma}(t)}{E_\mu}\quad(\mu = 1,2\ldots N). \tag{9}$$

One-dimensional creep, Eq. (9), can be efficiently solved with the unconditionally stable exponential algorithm, formulated for aging materials by [25]. If the right side of Eq. (9) remains constant, the time step $\Delta t = t_{n+1}-t_n$ may be increased arbitrarily, and so $\Delta t \gg \tau_{\min}$. The strain increment $\dot{\varepsilon}_\mu(t)$ in the μ-th Kelvin unit is obtained by integrating Eq. (8). After discretizing the continuous relaxation spectrum, one can formulate the following exponential algorithm for the B3 model

$$\Delta y_\mu = \Delta t\,/\,\tau_\mu \tag{10}$$

$$\lambda_\mu = \frac{1-\exp(-\Delta y_\mu)}{\Delta y_\mu} \tag{11}$$

$$\frac{1}{v_{n\,+\,1/2}} = q_2\left(\frac{\lambda_0}{t_{n+1/2}}\right)^m + q_3 \tag{12}$$

$$E'' = \left[q_1 + \frac{1}{v_{n+1/2}}\left(\sum_{\mu=\min}^{0}\frac{1}{E_\mu} + \sum_{\mu=1}^{\max}\frac{1-\lambda_\mu}{E_\mu}\right)\right]^{-1} \tag{13}$$

where the subscript $n+1/2$ refers to time $t_{n+1/2}$ at mid-step in log-time scale, i.e. the geometrical mean of t_n and t_{n+1}. Note that when the time step Δt is constant, Eq. (13) provides the same tangent incremental modulus E'' for non-aging material ($q_2=0$). Poisson's ratio is assumed to remain constant during creep, and so the incremental tangent stiffness tensor in three dimensions, $\mathbf{L}''$, may be assembled from E'' directly. The three-dimensional version of exponential algorithm is completed as follows

$$\Delta\boldsymbol{\varepsilon}'' = \frac{1}{v_{n+1/2}}\sum_{\mu=1}^{\max}[1-\exp(-\Delta y_\mu)]\boldsymbol{\gamma}_\mu^n + \frac{q_4}{t_{n+1/2}}\Delta t\boldsymbol{\sigma} \tag{14}$$

$$\Delta\boldsymbol{\sigma} = \mathbf{L}'' : (\Delta\boldsymbol{\varepsilon}-\Delta\boldsymbol{\varepsilon}'') \tag{15}$$

$$\boldsymbol{\gamma}_\mu^{n+1} = \boldsymbol{\gamma}_\mu^n\exp(-\Delta y_\mu) + \frac{\lambda_\mu E''}{E_\mu}(\Delta\boldsymbol{\varepsilon}-\Delta\boldsymbol{\varepsilon}'') \tag{16}$$

where strain tensor $\Delta\boldsymbol{\varepsilon}''$ represents an inelastic strain increment tensor corresponding to the history of loading, and $\boldsymbol{\gamma}_\mu$ are the internal tensor variables (or partial strains) of the Kelvin units which must be updated after each time step.

5. Microscale modeling via FFT-based method

The exponential algorithm was derived for a homogeneous continuum and must now be extended to a heterogeneous viscoelastic composite. The numerical homogenization techniques rely on replacing the real microstructure by a representative volume element (RVE) of the material. The RVE must be statistically representative, i.e., must be large enough to contain sufficient information about morphology, heterogeneities, etc. Moreover, the response of RVE

must be independent of the type of imposed boundary conditions, which favors larger RVE. An extensive numerical study [28] revealed that periodic boundary conditions yield the lowest dependence of the elastic homogenized stiffness on the RVE size.

The RVE of cement paste is here approximated by Bentz's discrete hydration model CEMHYD3D from the National Institute of Standards and Technology (NIST), which has the resolution of 1 μm [8]. Therefore, the periodic microstructure of cement paste is simulated on a grid of voxels $1\times1\times1$ μm in size. The hydration model captures the main chemical phases and reactions occurring during cement hydration, and has already furnished excellent results for elastic homogenization of hardened cement pastes with periodic boundary conditions [3].

The NIST model proved to have realistic correlation functions with real cement microstructures on large RVE $200\times200\times200$ μm [29]. However, the RVE $50\times50\times50$ presented further truncates cement particles above 19 μm in diameter, and the RVE $10\times10\times10$ even those above 5 μm. The previous results on the effective elasticity proved a weak sensitivity to the RVE size and particle truncation [30].

The macroscopic viscoelastic response of RVE is obtained through the solution of the local problem, which consists of the equilibrium and constitutive equations complemented by boundary conditions. According to the exponential algorithm, two equations must be satisfied in each time step

$$\operatorname{div}\,\Delta\boldsymbol{\sigma}(\mathbf{x}) = 0 \tag{17}$$

$$\Delta\boldsymbol{\sigma}(\mathbf{x}) = \mathbf{L}''(\mathbf{x}) : (\Delta\boldsymbol{\varepsilon}(\mathbf{x}) - \Delta\boldsymbol{\varepsilon}''(\mathbf{x})) = \mathbf{L}''(\mathbf{x}) : \Delta\boldsymbol{\varepsilon}(\mathbf{x}) - \Delta\boldsymbol{\lambda}(\mathbf{x}) \tag{18}$$

where inelastic strain increment $\Delta\boldsymbol{\varepsilon}''(\mathbf{x})$ is known from previous time step and can be replaced after multiplication with incremental stiffness tensor by eigenstress tensor $\Delta\boldsymbol{\lambda}(\mathbf{x})$. The periodic boundary conditions are expressed as decomposition of strain increments into average $\Delta\mathbf{E}$ and fluctuating part $\Delta\boldsymbol{\varepsilon}^*(\mathbf{x})$ over the RVE

$$\Delta\boldsymbol{\varepsilon}(\mathbf{x}) = \Delta\mathbf{E} + \Delta\boldsymbol{\varepsilon}^*(\mathbf{x}). \tag{19}$$

The usual way to solve the RVE equations such as Eqs. (17)–(19) has been the finite element method (FEM). It will be shown, however, that there is a better way—a method based on FFT, which has already met with success for some other civil engineering problems [31].

Following the idea of [32], we introduce a homogeneous reference medium with stiffness tensor $\mathbf{L}^0$. The incremental constitutive equation Eq. (18) can be written in the form

$$\Delta\boldsymbol{\sigma} = \mathbf{L}''(\mathbf{x}) : \Delta\boldsymbol{\varepsilon}(\mathbf{x}) - \Delta\boldsymbol{\lambda}(\mathbf{x}) = \mathbf{L}^0 : \Delta\boldsymbol{\varepsilon}(\mathbf{x}) + \Delta\boldsymbol{\tau}(\mathbf{x}) \tag{20}$$

where $\Delta\boldsymbol{\tau}(\mathbf{x})$ represents the stress polarization field, which already contains the contribution from eigenstress field and may be expressed as

$$\Delta\boldsymbol{\tau}(\mathbf{x}) = (\mathbf{L}''(\mathbf{x}) - \mathbf{L}^0) : \Delta\boldsymbol{\varepsilon}(\mathbf{x}) - \Delta\boldsymbol{\lambda}(\mathbf{x}). \tag{21}$$

The polarization stress field remains unknown, but can be related to the fluctuating strain field by means of convolution and translation-invariant Green operator $\boldsymbol{\Gamma}^0(\mathbf{x})$, which is explicit when the reference medium $\mathbf{L}^0$ is linearly elastic [31]

$$\Delta\boldsymbol{\varepsilon}^*(\mathbf{x}) = -\boldsymbol{\Gamma}^0(\mathbf{x}) * \Delta\boldsymbol{\tau}(\mathbf{x}). \tag{22}$$

Substitution of Eq. (22) into Eq. (19) and Eq. (21) yields

$$\begin{aligned}\Delta\boldsymbol{\varepsilon}(\mathbf{x}) &= \Delta\boldsymbol{E} - \boldsymbol{\Gamma}^0(\mathbf{x}) * \Delta\boldsymbol{\tau}(\mathbf{x}) = \\ &= \underbrace{\Delta\boldsymbol{E} + \boldsymbol{\Gamma}^0(\mathbf{x}) * (\mathbf{L}^0 : \Delta\boldsymbol{\varepsilon}(\mathbf{x}))}_{\Delta\boldsymbol{\varepsilon}(\mathbf{x})} - \boldsymbol{\Gamma}^0(\mathbf{x}) * \underbrace{(\mathbf{L}(\mathbf{x}) : \Delta\boldsymbol{\varepsilon}(\mathbf{x}) - \Delta\boldsymbol{\lambda}(\mathbf{x}))}_{\Delta\boldsymbol{\sigma}(\mathbf{x}) \text{ from Eq. (18)}}.\end{aligned} \tag{23}$$

This equation is the basis of a recursive iterative procedure ($k=0,1\ldots$)

$$\Delta\boldsymbol{\varepsilon}^{k+1}(\mathbf{x}) = \Delta\boldsymbol{\varepsilon}^k(\mathbf{x}) - \boldsymbol{\Gamma}^0(\mathbf{x}) * \Delta\boldsymbol{\sigma}^k(\mathbf{x}). \tag{24}$$

Note that local constitutive Eq. (18) needs to be called in each iteration to access $\Delta\boldsymbol{\sigma}^k(\mathbf{x})$.

The convolution in Eq. (24) may be efficiently evaluated by the FFT, which corresponds to multiplication in the Fourier space. For discretizing this equation, the periodic heterogeneous RVE may typically be subdivided into a three-dimensional lattice. To each node, called a Fourier point, we assign certain elastic or viscoelastic properties. In the CEMHYD3D microstructure model, each voxel represents such Fourier point. Once a near equilibrium state is reached, i.e. Eq. (24) is nearly satisfied, the macroscopic (or homogenized) stress and strain over the RVE can be expressed through volume averaging over Fourier points

$$\Delta\boldsymbol{\Sigma}^{k+1} = \langle\Delta\boldsymbol{\sigma}^{k+1}(\mathbf{x})\rangle = \frac{1}{V}\int_V \Delta\boldsymbol{\sigma}^{k+1}(\mathbf{x})dV \tag{25}$$

$$\Delta\mathbf{E}^{k+1} = \langle\Delta\boldsymbol{\varepsilon}^{k+1}(\mathbf{x})\rangle = \frac{1}{V}\int_V \Delta\boldsymbol{\varepsilon}^{k+1}(\mathbf{x})dV. \tag{26}$$

The selection of the reference stiffness tensor $\mathbf{L}^0$ affects the convergence rate. It is possible to choose the transformed reference stiffness tensor of the homogenized medium without encountering any numerical or iteration difficulties in the form

$$\mathbf{L}^{0,\mathrm{optim}}_{ijkl} = \frac{\alpha+\beta}{2}(\delta_{ik}\delta_{jl} + \delta_{il}\delta_{jk}) \tag{27}$$

where α and β denote the maximal and minimal eigenvalues of the stiffness tensors of all phases.

The intrinsic elastic properties used to assemble the isotropic stiffness tensors are summarized in Table 3. Two different forms of C-S-H, characterized by low or high density, as identified in [33], are listed as well. Both already contain short-time creep for the duration of unloading in nano-indentation tests (about 2.6 s~$3\cdot10^{-5}$ day).

Convergence of the FFT homogenization method to the prescribed macroscopic strain, $\Delta\mathbf{E}$, Eq. (19), is always assured. This is advantageous for the simulation of relaxation experiments, which are controlled by macroscopic strain. Creep experiments are controlled by macroscopic stress, which means that, in the first time step, $\Delta\boldsymbol{\Sigma}^0$ is equal to the macroscopic stress while, in the subsequent time steps, the stress increments are zero. Similarly, the unloading of RVE means imposing $-\Delta\boldsymbol{\Sigma}^0$ at n-th time step, to make the total zero macroscopic stress vanish. The iterative loop of the FFT method ($k=0,1,\ldots$) in Eq. (24) requires the desired macroscopic stress increment $\Delta\boldsymbol{\Sigma}^n$ at time step n to be converted into a macroscopic strain increment $\Delta\boldsymbol{E}^{k+1}$ in each k-th iteration step at constant time [34]

$$\Delta\boldsymbol{\Sigma}^n - \mathbf{L}^0 : \Delta\mathbf{E}^{k+1} = \langle\Delta\boldsymbol{\sigma}^k(\mathbf{x})\rangle - \mathbf{L}^0 : \langle\Delta\boldsymbol{\varepsilon}^k(\mathbf{x})\rangle. \tag{28}$$

Eq. (28) is valid only in equilibrium and can be rewritten as

$$\Delta\mathbf{E}^{k+1} = (\mathbf{L}^0)^{-1} : \left[\Delta\boldsymbol{\Sigma}^n - \langle\Delta\boldsymbol{\sigma}^k(\mathbf{x})\rangle + \mathbf{L}^0 : \langle\Delta\boldsymbol{\varepsilon}^k(\mathbf{x})\rangle\right]. \tag{29}$$

Searching for the macroscopic strain increment in each iteration leads to a greater number of iterations since $\Delta\mathbf{E}^{k+1}$ in Eq. (29) is evaluated from unequilibrated strain and stress fields. When dealing with extreme changes in viscous behavior in the RVE, one may observe oscillation of $\Delta\mathbf{E}^{k+1}$ with a decreasing amplitude.

The equilibrium iteration loop in Eq. (24) is terminated when the relative difference in the square norms over 50 cycles becomes less than 2%, that is,

$$0.98 \leq \frac{||\Delta \mathbf{E}^k||^2}{||\Delta \mathbf{E}^{k-50}||^2} \leq 1.02 \,. \tag{30}$$

This condition was verified to limit the relative error to less than 3% in strains per time step. Previously, a condition based on stress equilibrium [34] was used and was found to depend on the magnitude of the stress increment $\Delta\boldsymbol{\Sigma}^n$, which made it inappropriate for creep simulation.

The FFT-based method brings about four advantages over the FEM:

1) The computational time is relatively short (it is $0(N \log N)$ for one FFT iteration). For mature cement pastes, no more than 250 iterations in each time step are typically required, depending on the C-S-H viscous behavior.
2) An equally spaced grid of Fourier points can be directly used, and the grid can be taken directly from the RVE voxel representation without any need of meshing. Dividing one voxel into more Fourier points does not produce a significantly different macroscopic response for the contrast of elastic properties considered in this work.
   The latter is 55.1 for the bulk modulus and 167,300 for the shear modulus, disregarding empty porosity presented up to 9% by volume as the chemical shrinkage, Table 3. Previous study on hydrating cement paste showed that ergodic hypothesis of small RVE $10\times10\times10$ is invalid but averaging over five random realizations leads to similar macroscopic results [3] and is discussed more generally in [28,34] and later in Fig. 5.
3) The method converges to the theoretically exact solution, limited only by the number of iterations and samplings of RVE, except for heterogeneous materials with a high contrast of phases. Even for young cement paste, with water-filled porosity over 50% in volume, the FFT algorithm converged to correct solution but required more iterations.
4) The inelastic strain increments $\Delta\boldsymbol{\varepsilon}''$ need to be stored only at the creeping Fourier points. This is more efficient than the FEM, where $\Delta\boldsymbol{\varepsilon}''$ needs to be stored at each integration point assigned to the creeping body. In the case of a hexahedral element with tri-linear approximation functions, this requires eight storage places for such an element, instead of one in FFT.

5.1. FFT algorithm amalgamated with model B3

The solution of Eqs. (17)–(19) requires two computational loops: one running through the time steps ($n=0,1\ldots$), and the second one iterating for equilibrium ($k=0,1\ldots$). When the exponential algorithm for a general three-dimensional stress is combined with model B3 (which includes aging), one obtains the following algorithm for the simulation of a creep test:

(1) At the beginning of calculation ($t=t'$), specify the number of Kelvin units and the relaxation times $\tau_{\min}\ldots\tau_0\ldots\tau_{\max}$. At each Fourier point in C-S-H, set the internal variables $\boldsymbol{\gamma}_\mu^0(\mathbf{x})$ and the total stress $\boldsymbol{\sigma}^0(\mathbf{x})$ equal to zero tensors.
(2) Assemble stiffness tensors $\mathbf{L}(\mathbf{x})$ from Table 3. Find the reference homogeneous medium $\mathbf{L}^0$, Eq. (27). Calculate the stiffness moduli of non-aging Kelvin units E_μ, Eqs. (6) and (7).
(3) For the given time step $\Delta t = t_{n+1} - t_n$ ($n=0,1\ldots$), specify the macroscopic stress increment $\Delta\boldsymbol{\Sigma}^n$ to be satisfied as the result of FFT iteration, Eq. (29). Assign macroscopic trial strain $\Delta\mathbf{E}^0$ to $\Delta\boldsymbol{\varepsilon}^0(\mathbf{x})$ at all Fourier points. Evaluate Δy_μ and λ_μ for each Kelvin spring-damper unit at each Fourier point from Eqs. (10) and (11), the aging function $1/v_{n+1/2}$ in Eq. (12), and the total incremental modulus E'' for Kelvin chain with elastic spring, including aging, Eq. (13). Then update the tangent stiffness tensor $\mathbf{L}(\mathbf{x})$ at each Fourier point based on E'', Eq. (13), and constant Poisson's ratio v. The extreme values of E'' ranged from $E((t-t)'=0)''=29.4$ GPa to $E((t-t')=1000$ days)"$=8.8$ GPa as obtained later from an inverse analysis.
(4) Compute the inelastic strain increment $\Delta\boldsymbol{\varepsilon}(\mathbf{x})$ in all creeping points, Eq. (14). Use the total stress tensor from the last time step to quantify the flow term.
(5) Start the FFT iteration loop ($k=0,1\ldots$) with the discrete Fourier frequencies $\boldsymbol{\xi}_j$ ($j=1,2\ldots$) for the stress and strain fields at all Fourier points.
   (a) Initialize the trial stress field for the FFT algorithm at all Fourier points only when $k=0$

$$\Delta\boldsymbol{\sigma}^0(\mathbf{x}) = \mathbf{L}''(\mathbf{x}) : [\Delta\boldsymbol{\varepsilon}^0(\mathbf{x}) - \Delta\boldsymbol{\varepsilon}''(\mathbf{x})]. \tag{31}$$

   (b) Transform $\Delta\boldsymbol{\sigma}^k(\mathbf{x})$ by means of FFT[1] to $\widetilde{\Delta\boldsymbol{\sigma}}^k(\boldsymbol{\xi}_j)$ and set

$$\widetilde{\Delta\boldsymbol{\varepsilon}}^{k+1}(\boldsymbol{\xi}_j) = \widetilde{\Delta\boldsymbol{\varepsilon}}^{k}(\boldsymbol{\xi}_j) - \widetilde{\boldsymbol{\Gamma}}^0(\boldsymbol{\xi}_j) : \widetilde{\Delta\boldsymbol{\sigma}}^k(\boldsymbol{\xi}_j), \quad \forall \boldsymbol{\xi}_j \neq 0 \tag{32}$$

$$\widetilde{\Delta\boldsymbol{\varepsilon}}^{k+1}(\boldsymbol{\xi}_j) = \Delta\mathbf{E}^k, \forall \boldsymbol{\xi}_j = 0. \tag{33}$$

   (c) Transform $\widetilde{\Delta\boldsymbol{\varepsilon}}^{k+1}(\boldsymbol{\xi}_j)$ by means of inverse FFT[1] to $\Delta\boldsymbol{\varepsilon}^{k+1}(\mathbf{x})$.
   (d) Calculate the quasi-static stress increment at each Fourier point

$$\Delta\boldsymbol{\sigma}^{k+1}(\mathbf{x}) = \mathbf{L}''(\mathbf{x}) : [\Delta\boldsymbol{\varepsilon}^{k+1}(\mathbf{x}) - \Delta\boldsymbol{\varepsilon}''(\mathbf{x})]. \tag{34}$$

   (e) Compute the average stress and strain tensors, both for updated $k+1$, Eqs. (25) and (26).
   (f) If the equilibrium condition Eq. (30), is met, jump to item 6.
   (g) Determine the new macroscopic strain tensor $\Delta\mathbf{E}^{k+1}$ that approaches the required macroscopic stress tensor $\Delta\boldsymbol{\Sigma}^n$ according to Eq. (29). If a creep test with constant stress is to be simulated, set $\Delta\boldsymbol{\Sigma}^n = \mathbf{0}$ for $n>0$. Return to point 5b).
(6) Eq. (34) is approximately satisfied, i.e., the state is near enough to equilibrium. Therefore, update the internal variables $\boldsymbol{\gamma}_\mu^{n+1}(\mathbf{x})$ according to Eq. (16), update the total local strain $\boldsymbol{\varepsilon}^{n+1}(\mathbf{x})$ and the stress $\boldsymbol{\sigma}^{n+1}(\mathbf{x})$ by adding increments $\Delta\boldsymbol{\varepsilon}^{k+1}(\mathbf{x})$ and $\Delta\boldsymbol{\sigma}^{k+1}(\mathbf{x})$. Update total macroscopic stress $\boldsymbol{\Sigma}^{n+1}$ and strain $\mathbf{E}^{n+1}$ by adding increments $\Delta\boldsymbol{\Sigma}^{k+1}$ and $\Delta\mathbf{E}^{k+1}$.
(7) Return to item 3 and analyze the next time step, if required.

A comment is in order regarding the control of the required macroscopic strain or stress during homogenization. The FFT-based method always converges to the prescribed $\Delta\mathbf{E}^k$. The macroscopic creep response is controlled by $\Delta\boldsymbol{\Sigma}^0$, and so $\Delta\mathbf{E}^k$ must be calculated at each time step and in each iteration, Eq. (29). For example, let the macroscopic homogenized Young's modulus of RVE be 20 GPa with Poisson's ratio $v=0.3$. We want to simulate uniaxial creep with $\boldsymbol{\Sigma}_{11}=1.0$ GPa. To produce a unit stress in the x direction, a suitable choice of trial strain tensor $\Delta\boldsymbol{E}^0$, corresponding to the elastic response at the first loading cycle, is $\Delta E_{11}^0 = 0.05$, $\Delta E_{22}^0 = \Delta E_{33}^0 = -0.015$. Such an initial guess significantly improves iterations in the FFT loop aimed to achieve the desired value of $\boldsymbol{\Sigma}_{11}$.

The verification is carried out on the homogeneous RVE $10\times10\times10$ made from C-S-H. The input parameters for C-S-H are taken from the left column of Table 2. The starting trial strain $\Delta\mathbf{E}^0$ is chosen as the zero tensor, which obviously makes no sense but shows the robustness of the method. The macroscopic strain is plotted after 10, 20 and 50 iterations in Fig. 1. Note that a more realistic selection of

[1] Using open source package fftw, version 2.1.3.

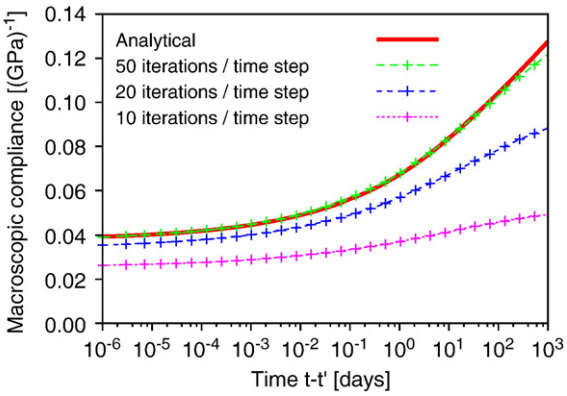

Fig. 1. Verification of FFT method for homogeneous viscoelastic RVE $10\times10\times10$ μm assembled from C-S-H voxels.

$\Delta \boldsymbol{E}^0$ significantly improves the convergence. The analytical solution can be found in [23].

5.2. Sensibility of FFT method to resolution

Moulinec and Suquet [34] demonstrated a low sensitivity of this method to spatial resolution. Giving a continuous description of a circular fiber in a matrix, they were increasing the resolution so that a digitized image converged to the continuous representation. The error remained below 1% for the effective elastic properties with the maximum contrast 6.3 for the shear moduli and approximately equal volume fractions of two phases. Such a good elastic performance is the result of (i) reasonable stress-strain approximation with even a few Fourier points, (ii) smooth boundaries, and (iii) a low contrast of properties.

Due to the lack of fine and real image for a cement paste a different sensibility test is adopted. The RVE $50\times50\times50$ from Fig. 3 is taken from the CEMHYD3D model as a representative of a mature cement paste; this RVE is based on the cement described in the next sections. Each voxel is subdivided two and four times in order to produce $100\times100\times100$ and $200\times200\times200$ RVEs. Table 3 summarizes the assigned elastic properties and the left column of Table 2 the parameters for C-S-H with $q_4=0$. The porosity remains empty in order to boost the phase contrast being five orders of magnitude for bulk and shear moduli. Two cases are computed to elucidate the contrast of properties; C-S-H Young's modulus with 26.25 GPa and 5.0 GPa.

Table 1 summarizes the static effective response after 300 iterations. The maximum relative difference is 9% for bulk moduli. Generally, $50\times50\times50$ produces the lowest bulk modulus and the highest shear modulus in the comparison with larger RVE sizes. The results clearly demonstrate a good description of the overall strain field fluctuation. The voxel refinement to more Fourier points preserves the lowest frequencies dominating the overall response. Fine details introduce high frequencies, being insignificant in nonlocalized analysis such as viscoelasticity. In this particular case of mature paste, the size $50\times50\times50$ is sufficient for the expected error of a few percent.

5.3. Inverse creep analysis for two-year old cement paste

The irreversible creep of C-S-H will be obtained from the unloading stage of a two-year old hardened cement paste, with water–cement ratio of w/c = 0.5 [35]. An ordinary Portland cement was used, having Bogue composition C_3S (46.5), C_2S (24.6), C_3A (10.4), and C_4AF (8.3), and Blaine fineness of 340 m^2/kg. The test cylinders were stored in lime water for two years at 22 °C and then subjected to sustained load with stress/strength ratio 0.3. Pairs of "T-shape" beams were cut from the stored cylinders, Fig. 2, and subjected to axially compressive load 10.35 MPa in a humidity-controlled chamber, which was maintained at 96% relative humidity (RH) instead of 100% due to technical difficulties. After 72 h, the specimens were unloaded. Drying shrinkage was measured on a companion load-free specimen.

Two RVEs $10\times10\times10$ and $50\times50\times50$ μm of cement paste were reconstructed using the CEMHYD3D model. Fig. 3 shows them at the time of two years. The chemical composition of clinker was normalized according to the aforementioned data, and the cement particle size distribution was taken to be the same as for reference cement 16132 with Blaine fineness of 357 m^2/kg and autocorrelation files from reference cement 115 of NIST database, see [8]. The gypsum content was assumed to be 5% by volume. The CEMHYD3D simulation reached the 0.988 degree of hydration, for which the important volume fractions were as follows: calcium hydroxide 0.141, C-S-H_{LD} 0.303, C-S-H_{HD} 0.183, unhydrated clinker mineral 0.004, water-filled capillary porosity 0.199, and empty capillary porosity 0.003 caused by inaccessibility of certain parts of the RVE to pore water even at saturated curing conditions. The ratio C-S-H_{HD}/(C-S-H_{HD} + C-S-H_{LD}) was 0.376, which agrees well with the J–T model [20].

The specimens were simultaneously in the process of drying to the RH of 96%. The measured shrinkage strain [36] was fitted by the equation [1,9]

$$\varepsilon_{sh}(t) = 0.165\tanh\sqrt{\frac{(t-t')-0.1}{\tau_{sh}}},\ (t-t')\geq 0.1\,\text{day} \tag{35}$$

where 0.1 day is the time at which drying began to have an effect on the specimen, and $\tau_{sh}=0.8$ day is the shrinkage half-time, Fig. 4. The uncertainties in Eq. (35) have only a small effect on the irrecoverable strain after unloading. For simplicity, it is assumed, as usual, that shrinkage and creep strain are additive, even though this is not exactly true, Eq. (4).

To simplify the analysis, C-S-H_{LD} and C-S-H_{HD} were merged into a single C-S-H phase. The average elastic properties of both kinds of C-S-H were calculated via the Mori–Tanaka method, yielding average Young's modulus of 24.31 GPa and Poisson's ratio of 0.24, when the reference phase was C-S-H_{LD}. Parameters q_1,q_3,q_4,λ_0,n for the C-S-H creeping phase in model B3 are unknown. Parameter q_4 quantifies the irrecoverable flow strain which can be determined from unloading, independently of the other parameters of mature paste. Parameters q_1 and q_3 are in fact related through nano-indentation data, but are subjected to a certain range of uncertainty, limited by the creep attained.

The nano-indentation data provide a C-S-H indentation modulus that includes short-term creep. When the unloading duration of

Table 1
Effective properties reflecting voxel subdivision into Fourier points.

Effective modulus	Bulk	Shear	Young's	Bulk	Shear	Young's
C-S-H Young's modulus	$E=26.25$ GPa			$E=5.0$ GPa		
$50\times50\times50$	9.529	6.620	16.125	3.363	2.304	5.626
$100\times100\times100$	9.689	6.170	16.267	3.575	2.267	5.613
$200\times200\times200$	9.786	6.162	15.279	3.669	2.259	5.623

Each voxel in initial $50\times50\times50$ is subdivided two and four times. Values are for 300 iterations in GPa.

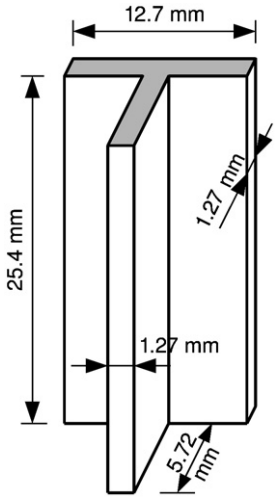

Fig. 2. "T" shape bar used in creep and shrinkage tests of cement pastes [18].

nano-indentation is assumed to be 2.6 s, the C-S-H compliance $J(t' + 3{\cdot}10^{-5}\,\text{day},t)$ is known.

Parameter λ_0 controls the time at the middle of the transition from power-law to logarithmic creep curve, and was assumed to be 1 day, as found in fitting model B3 to extensive test data [23]. Parameter n controls the curvature of creep curve in the logarithmic plot and has a strong effect. In view of the aforementioned influences, the parameter values were chosen as summarized in Table 2. The main point is the value of q_4, determined from unloading data.

Fig. 4 shows the viscoelastic behavior assigned to C-S-H, both with and without flow term ($q_4 = 0$), to illustrate the effect of irrecoverable creep part. An arrow points to the time when the indentation modulus is typically evaluated. The asymptotic compliance $q_1 = 0.0381\ \text{GPa}^{-1}$ is about 93% of compliance from nano-indentation data $J(t + 0.00003\ \text{day}, t) = 0.0411\ \text{GPa}^{-1}$. The elastic strain immediately after loading was not reported [35] and was assumed to be $800{\cdot}10^{-6}$ for static load 10.35 MPa at 0.01 day, Fig. 4. The choice has a negligible effect on the data after unloading when elastic strain is immediately recovered.

The irrecoverable strain from the simulation is $17.1{\cdot}10^{-6}$ at 100 days after unloading, which is 1.8% of the maximum attained viscoelastic strain $954{\cdot}10^{-6}$. The result is consistent with Parrot [37] who found that the irrecoverable part of creep decreases with increasing maturity, which may be due progressive polymerization of C-S-H, accelerated by heat curing. In our particular case, the polymerization of C-S-H causes aging.

As shown in Table 1, the FFT method is weakly sensitive to the voxel subdivision. The question about the appropriate RVE size underlining the ergodic hypothesis remains. Fig. 5 elucidates such effect on the paste compliance. Five random representations $10\times10\times10$ and $50\times50\times50$ were generated with the same assigned viscoelastic properties. The size $50\times50\times50$ gives a negligible scatter while $10\times10\times10$ shows significant variation. All responses are rather parallel meaning that the elasticity itself determines the viscous behavior. Also, it becomes possible to substitute $50\times50\times50$ with a carefully selected $10\times10\times10$. In agreement with [28], the mean response in small and big size representations coinsides due to the periodic boundary conditions. The RVE $50\times50\times50\ \mu\text{m}$ is obviously sufficient.

The homogenization of $10\times10\times10$ (or $50\times50\times50$) RVE took maximally 3.6 MB (or 104 MB) of computer memory. The total computation time was 1 min (or 100 min) on 3.2 GHz CPU, 34 (or 34) time steps, 6850 (or 6550) total iterations, with an average time per iteration of 9 ms (or 0.92 s), and an average number of iterations per time step of 201 (or 192).

5.4. Inverse basic creep analysis of 30-year old cement paste

The same "T" specimens, Fig. 2, made from the same cement, but now aged for 30 years, were loaded uniaxially in a basic creep experiment at the stress level of 0.3 of the compressive strength [18]. The temperature of water bath used for curing was 24 °C. Therefore, the same RVE $50\times50\times50$ was assumed since the hydration has stopped long ago. A certain change in the microstructure might have been caused by the shrinkage of aging C-S-H and by variation of C-S-H density with temperature; but these scenarios are disregarded.

Tamtsia and Beaudoin [18] explored the effect of water resaturation on the basic creep properties. Prior to the basic creep experiment, certain specimens were D-dried or dried to 42% RH and then resaturated. According to model B3, drying and resaturation treatment induces microprestress, which affects the flow term only. In the inverse C-S-H analysis, the aim was to match, for the same C-S-H, the experimental data with different flow terms only. The saturated specimens should yield a very low flow strain, if any, while the resaturated specimens should exhibit a larger creep strain due to induced microprestress, hence, an increased flow term.

As it turned out, Young's modulus of C-S-H must be increased in order to get a better match of the early creep data. No other B3 parameter can help to reduce the compliance at short creep duration. We assumed the compliance $J(t + 0.00003\ \text{day}, t) = 1/29.4\ \text{GPa}^{-1}$, corresponding to C-S-$H_{HD}$ nano-indentation data, Table 3. Furthermore, based on previous experiments, we assumed $q_4 = 0.002\ \text{GPa}^{-1}$ for saturated specimens, for which irreversible shrinkage is small.

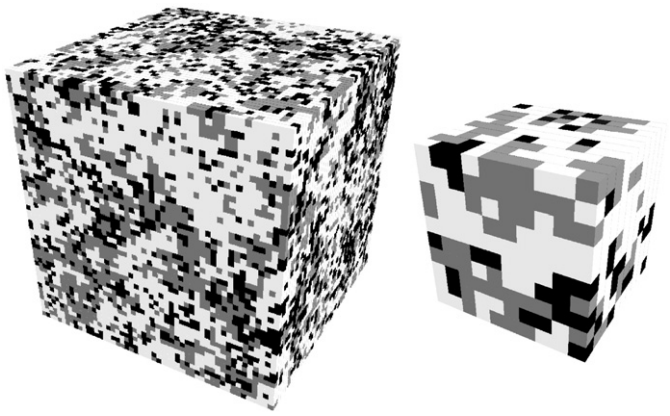

Fig. 3. RVE of cement paste $50\times50\times50$ (left) and $10\times10\times10\ \mu\text{m}$ (right). White = C-S-H (viscoelastic), grey = other solids (elastic), and black = porosity.

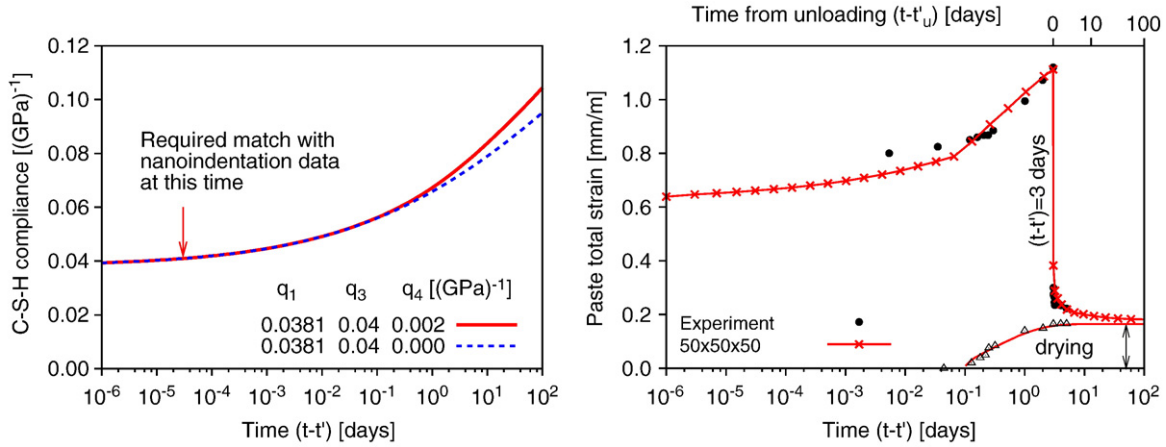

Fig. 4. Compliance assigned to C-S-H (left), for comparison without the flow term ($q_4 = 0$). Measured total strain of two-year old cement paste (right) with simulated strain for two RVE sizes.

Thus two parameters q_3 and n must be identified for basic creep on a saturated specimen.

Fig. 6 shows the C-S-H creep from experiments and the corresponding homogenized creep at the level of cement paste. To match the attenuation of creep rate, which was slower than for concrete, parameter n had to be increased, Table 2. All the experimental results with different drying histories were successfully matched while changing q_4 only. Fig. 6 shows also the creep strain after unloading even though it was not measured.

The comparison between ESEM images from virgin paste and after drying shrinkage gave access to the maps of drying shrinkage [38]. Strains over 25% were not exceptions when drying from RH 90% to 50%. No visible cracks have formed but regions of rarefactions were commonly observed [38]. Closer examination of Fig. 6 reveals that the initial compliance in basic creep is very similar, regardless of drying history. This means that resaturation made the C-S-H phase swelling to its original shape, eliminating rarefaction regions and closing possible microcracks. Such a conclusion is important in regard to assumed perfect bonding among phases in the homogenization process.

The micromechanical analysis makes it possible to access the stress at micrometer level. Fig. 7 shows the stress redistribution for saturated cement paste. The RVE was loaded macroscopically by 1 MPa in one direction and the average stress in the same direction was calculated. The averaging was performed over the whole RVE, i.e., the total sum of stress in the considered phase was divided by the RVE volume. Then the average stress from the C-S-H, other solids and pores must give back 1 MPa. The compliance behavior of C-S-H is manifested by progressive redistribution of the macroscopic stress to other elastic phases, Fig. 7. Once the RVE is unloaded, the deformed elastic phases aim to regain their original shape. Consequently, the C-S-H must get loaded for a short period in tension until all the recoverable creep has taken place. After a long time, all the phases will finish with a near-zero stress but the C-S-H will possess permanent strain due to C-S-H flow.

Table 2
Assigned C-S-H parameters and homogenization details in the analysis of non-aging 2 and 30 year old cement pastes.

Experiment	2 year old paste	30 year old paste
q_1 [$(GPa)^{-1}$]	0.0381	0.0326
q_2 [$(GPa)^{-1}$]	0.0	0.0
q_3 [$(GPa)^{-1}$]	0.040	0.050
q_4 [$(GPa)^{-1}$]	0.002	0.002, 0.018, 0.040[a]
m [−]	No effect	No effect
n [−]	0.25	0.35
λ_0 [day]	1	1
$1/J(t+2.6\,s,t)$ C-S-H [GPa][b]	24.31	29.4
Poisson's ratio of C-S-H [−]	0.24	0.24
t' [day][c]	1	1
Kelvin units	11	11
τ_1 [day]	10^{-7}	10^{-7}
τ_{max} [day]	10^3	10^3
Max. attained iterations	300	300

[a] Parameters for saturated, dried to 42% RH and D-dried samples.
[b] Approximately corresponding to Young's modulus from nano-indentation data.
[c] Due to non-aging creep takes effect only in microprestress (flow) term.

6. Discussion

The present analysis of the mature cement paste is not exhaustive, and thus the obtained parameters cannot be claimed to be unique. However, the clear physical meaning of model B3 parameters gives an idea of their meaningful ranges, which indicate the most likely values. Since linear elasticity governs the short-time creep, the homogenization suffers from almost no bias due to the viscous parameters identified for the C-S-H.

6.1. Compressibility of capillary water

The closed system of a single RVE does not allow water to migrate out or in, through the RVE boundaries. The hydrostatic stress of water in the capillary pores is insignificant, as shown in Fig. 7 for the 30-year old cement paste. Therefore, the hydrostatic stress of water cannot play a significant role in creep deformation at the microscale. A different behavior may be expected for young cement pastes.

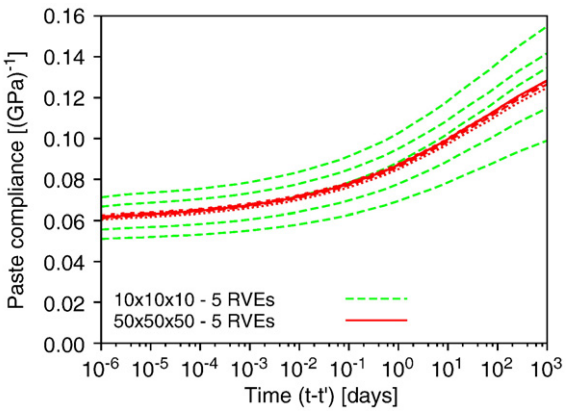

Fig. 5. Compliance of two-year old cement paste depending on random realization. Five representations were generated for each $10\times10\times10$ and $50\times50\times50$.

Table 3
Intrinsic elastic properties of chemical phases as measured by nano-indentation or mechanical tests with standard deviation.

Chemical phase[a]	Young's modulus [GPa]	Poisson's ratio [−]	Reference
C_3S	**135** ± 7	**0.3**	[14]
C_2S	**130** ± 20	**0.3**	[14]
C_3A	**145** ± 10	**0.3**	[14]
C_4AF	**125** ± 20	**0.3**	[14]
$\bar{C}S\bar{H}_2$	16–**30**–35	0.18–**0.3**–0.34	[46]
Water-filled porosity[b]	**0.001**	**0.499924**	–
Empty porosity	**0.001**	**0.001**	–
Calcium hydroxide	**38** ± 5	**0.305**	[2]
C-S-H_{LD}	**21.7** ± 2.2	**0.24**	[33]
C-S-H_{HD}	**29.4** ± 2.4	**0.24**	[33]
$C_6A_{\bar{S}3}H_{32}$	**22.4**	**0.25**	[47]
$C_4A\bar{S}H_{12}$	**42.3**	**0.324**	[47]
C_3AH_6	**22.4**	**0.25**	Estimated from [47]
FH_3	**22.4**	**0.25**	Estimated from [47]

Bold values are used in the homogenization.
[a] Using standard cement nomenclature.
[b] Bulk modulus of 2.19 GPa.

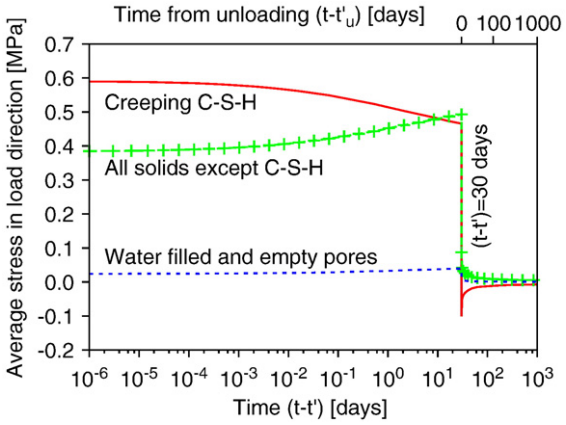

Fig. 7. Average stress and its redistribution among phases in the direction of imposed load. Results from FFT homogenization on saturated cement paste during basic creep, w/c = 0.5.

Overall, the paste permeability is controlled to a great extent by the fraction of pore space representing the capillary porosity. When it is decreased below a certain fraction (typical of modern concretes), the capillaries loose continuity [39]. This means that water molecules must pass through the nanoscale pores, which thus control permeability and cause the permeability to drop by orders of magnitude (see section on "Saturation Transition" in [40], and also [41]).

Recently, in more details, Bentz et al. [42] showed that w/c = 0.5, giving capillary porosity fraction between 0.17 and 0.23, produces what they call the capillary depercolation threshold, which they find to depend on the cement grain size distribution. For example, the asymptotic Young's modulus of the two-year old cement paste considered here in FFT homogenization is 16.15 GPa, and the bulk modulus is 11.69 GPa. When water is deactivated, the bulk modulus drops by 18.4% to 9.537 GPa. In this particular case, the capillary porosity of 0.202 is close to the depercolation threshold (implied in [40]). So the paste permeability must be controlled by low-permeable C-S-H rather than by capillary porosity.

In the present creep experiments, the macroscopic volumetric stress is 1/3 of the applied uniaxial stress. Therefore, the reduction of macroscopic creep strain due to water deactivation will be approximately a third of 18.4%. Fig. 8 shows the differences in the evolution of macroscopic strain for undrained conditions. The ratio of both strains remains indeed below 7% during all loading stages. The drained conditions, if applied in the inverse analysis, would bring slightly different C-S-H parameters but would not cause any divergence of results. So, it appears that, if all the experimental and material uncertainties are considered, determination of the undrained conditions would bring about the same error magnitude as for mature cement paste.

6.2. Constant Poisson ratio for C-S-H

The introduction of a constant Poisson ratio for C-S-H necessarily implies coupling between the volumetric and deviatoric creep mechanisms. Creep may be assumed to be is linked to adsorbed water in the hydrates migrating to capillary pores on the scale between 10 nm and 50 μm [43]. It appears plausible that not only the deviatoric (or shear) creep buy also the volumentric creep are caused by slips and restoration of bonds between two adjacent sheets of C-S-H. Migration of adsorbed water along nanopores between C-S-H sheets destabilizes the vad der Waals bonds between the sheets. The multiaxial creep experiment on a leached cement paste proved that the Lagrangian porosity decreases during roughly the first three weeks of loading. Much smaller volumetric creep occurred afterwards [44].

Unfortunately, distinct mechanisms of volumetric and deviatoric creep of C-S-H cannot be addressed with CEMHYD3D's resolution of 1 μm. The lack of multiaxial experimental data for mature cement pastes is another pragmatic reason why the Poisson ratio of C-S-H has been assumed as constant.

The effect of volumetric and deviatoric creep components is exemplified by the strain energy density determined at the initial load

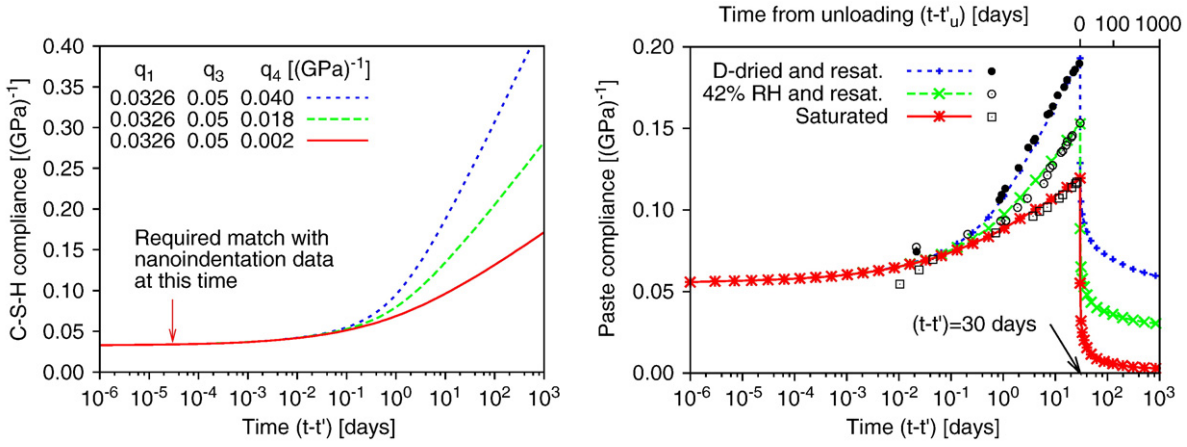

Fig. 6. Compliance assigned to C-S-H (left), for comparison without the flow term ($q_4 = 0$) and simulated and measured total strains of 30-year old cement paste for two RVE sizes (right).

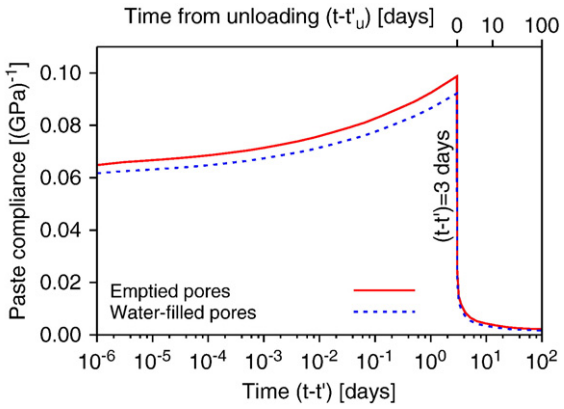

Fig. 8. Difference in creep compliance when capillary water is deactivated. C-S-H creep parameters from Table 2, two-year old cement paste, w/c = 0.5.

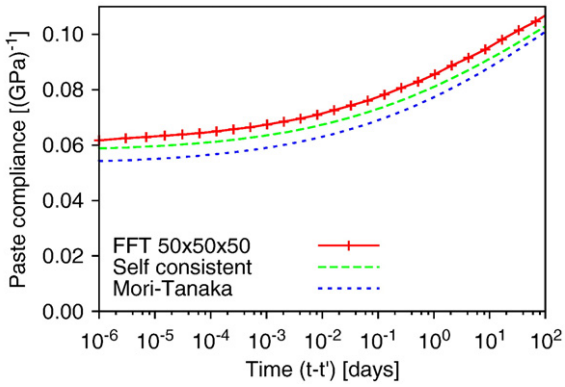

Fig. 9. Comparison of FFT-based and analytical methods. C-S-H creep parameters from Table 2 without flow term, two-year old cement paste, w/c = 0.5.

step. For linear elastic materials, the decomposition into volumetric and deviatoric parts reads:

$$W = \frac{1}{2}\boldsymbol{\varepsilon} : \mathbf{L} : \boldsymbol{\varepsilon} = \frac{9}{2}K\varepsilon_V^2 + G(\boldsymbol{\varepsilon} - \varepsilon_V\boldsymbol{\delta}) : (\boldsymbol{\varepsilon} - \varepsilon_V\boldsymbol{\delta}) \tag{36}$$

$$\varepsilon_V = \varepsilon_{ii}/3. \tag{37}$$

The ratio of deviatoric to volumetric energy is 11.2, based on the average strain C-S-H energy and produced by the uniaxial load initially applied on the two-year old cement paste. In this particular case, the deviatoric strain governs the creep response which also involves a volumetric strain.

6.3. Comparison with analytical viscoelastic homogenization

The numerical results obtained by the FFT method are compared with an approximate analytical solution. If Eq. (4) is recast for a non-aging and flow-free material and is expressed as a convolution in Laplace–Carson domain for a composite phase r, one has

$$\boldsymbol{\varepsilon}_r(t) = \int_0^t \mathbf{J}_r(t-t')\mathbf{d}\boldsymbol{\sigma}_r(t') \tag{38}$$

$$\boldsymbol{\varepsilon}_r(s) = \mathbf{J}_r(s) * \boldsymbol{\sigma}_r(s) \tag{39}$$

Eq. (39) resembles formally the equations of elasticity in Laplace–Carson domain, which is known as the correspondence principle. After a homogenization of elastic type in the Laplace–Carson domain, the effective properties are transformed to the time domain via Gaver–Stehfest algorithm [45].

Two analytical methods heavily used in the homogenization of cement-based materials are employed. They are based on the volume fractions of material phases, and on the Mori–Tanaka and self-consistent schemes for isotropic materials [44]. The two-year old cement paste is simulated as a viscoelastic composite with a creeping C-S-H phase for which the parameters are given in Table 2 with a zero flow term ($q_4 = 0$). The Mori–Tanaka method considers the C-S-H matrix as the reference medium. Fig. 9 demonstrates that all the three methods give similar results. This similarity is explained by a low total porosity (0.202) and by the dominance, in mature cement paste, of the C-S-H fraction (which is 0.486).

7. Conclusions

(1) Micromechanics could potentially bring significant benefits for predicting the macroscopic creep of cement paste and concrete if the creep properties of the C-S-H phase on the microscale were known. The present study aims to identify these properties.

(2) The basic hypothesis of this study is that the C-S-H is the only phase responsible for macroscopic creep. This hypothesis is supported by short-term nano-indentation data.

(3) The present numerical FFT-based method provides a powerful and robust tool for homogenization of viscoelastic heterogeneous material. This method is here exploited for inverse analysis of the heterogeneous composition of hardened cement paste, intended to shed light on the creep properties of C-S-H without its pores (which are anyway inaccessible to direct measurement). Compared to the FEM, the advantage is higher accuracy and low demand on computer memory. Analysis of random realizations and FFT sensibility to resolution indicated that the RVE of $50 \times 50 \times 50$ μm is sufficient.

(4) The inverse analysis assumes that C-S-H has a constitutive law of the same form as model B3 for concrete, but with modified parameters. All the simulations reveal that C-S-H must exhibit a slower decay of creep rate with time than does the cement paste or concrete. In other words, the positive curvature of the rising creep curve in the logarithmic time scale must be higher for C-S-H, and so must the exponent n of the long-time asymptotic power law for creep strain (calculations indicate that $n \approx 0.35$ instead of 0.1). This phenomenon can be explained by gradual stress redistribution among the phases of cement paste, in which a part of the applied load is gradually transferred to the non-creeping phases such as the portlandite or unhydrated clinker minerals.

(5) The irreversible basic creep of a two-year old cement paste is small. After 100 days of recovery following 3 days of creep under load, it represents only a few percent of the maximum strain observed.

(6) The macroscopic response identified from the analysis of C-S-H is micromechanically reasonable.

(7) Resaturation of dried 30-year old cement paste specimens leads to an increase in basic creep, compared to an initially saturated specimen. The inverse analysis showed that, among the C-S-H parameters, only the flow (or irreversible) strain needs to be considered to depend on the history of drying. Such behavior is consistent with the microprestress theory. It transpires that the microprestress induced by drying controls only the flow term of creep.

(8) The homogenization procedure in this study is limited to old and mature cement pastes, in which hydration and aging have already ceased. The extension to early ages, which is more important to the engineering community, is in principle possible if the homogenization procedure is coupled with a hydration model. However, more fundamental information

about C-S-H would be needed. Quantification of irreversible shrinkage will also be important.

Acknowledgments

Partial financial supports under the grant GA103/08/1492 "Virtual tests of concrete" to the Czech Technical University, and under the U.S. National Science Foundation grant CMS-0556323 to Northwestern University, are gratefully acknowledged. The latter grant also provided support for V. Šmilauer's Visiting Scholar appointment at Northwestern University.

References

[1] Z. Bažant, S. Baweja, Creep and shrinkage prediction model for analysis and design of concrete structures: Model B3, Tech. rep., Am. Concrete Institute, 2000.
[2] O. Bernard, F.-J. Ulm, E. Lemarchand, A multiscale micromechanics-hydration model for the early-age elastic properties of cement-based materials, Cem. Concr. Res. 33 (9) (2003) 1293–1309.
[3] V. Šmilauer, Z. Bittnar, Microstructure-based micromechanical prediction of elastic properties in hydrating cement paste, Cem. Concr. Res. 36 (9) (2006) 1708–1718.
[4] Z.C. Grasley, D.A. Lange, The viscoelastic response of cement paste to three-dimensional loading, Mech. Time-Depend. Mater. 11 (2007) 27–46.
[5] L. Granger, Z. Bažant, Effect of composition on basic creep of concrete and cement paste, J. Eng. Mech. ASCE 121 (11) (1995) 1261–1270.
[6] S. Baweja, G. Dvorak, Z. Bažant, Triaxial composite model for basic creep of concrete, J. Eng. Mech. ASCE 124 (9) (1998) 959–966.
[7] Ch. Pichler, R. Lackner, A multiscale creep model as basis for simulation of early-age concrete behavior, Computers and Concrete 5 (4) (2008) 295–328.
[8] D.P. Bentz, CEMHYD3D: A Three-Dimensional Cement Hydration and Microstructure Development Modeling Package. Version 3.0., Tech. rep., NIST Building and Fire Research Laboratory, Gaithersburg, Maryland (2005).
[9] S. Baweja, Z. Bažant, Creep and shrinkage prediction model for analysis and design of concrete structures — model B3, materials and structures, 28 (6, RILEM, Paris, 1995, pp. 357–365.
[10] Z. Bažant, S. Baweja, Justification and refinement of Model B3 for concrete creep and shrinkage. 1. Statistics and sensitivity, Mater. Struct. 28 (7) (1995) 415–430.
[11] Z. Bažant, S. Baweja, Justification and refinement of Model B3 for concrete creep and shrinkage. 2. Updating and theoretical basis, Mater. Struct. 28 (8) (1995) 488–495.
[12] Z. Bažant, Viscoelasticity of porous solidifying material—concrete, J. Eng. Mech. Div. ASCE 103 (1977) 725–728.
[13] H.M. Jennings, Colloid model of C-S-H and implications to the problem of creep and shrinkage, Mater. Struct. 37 (1) (2004) 59–70.
[14] K. Velez, S. Maximilien, D. Damidot, G. Fantozzi, F. Sorrentino, Determination by nanoindentation of elastic modulus and hardness of pure constituents of Portland cement clinker, Cem. Concr. Res. 31 (2001) 555–561.
[15] H. Jennings, J. Thomas, J. Gevrenov, G. Constantinides, F.-J. Ulm, Nanostructure of C-S-H gel in cement paste as a function of curing conditions and relative humidity, International Conference on Creep, Shrinkage and Durability of Concrete and Concrete Structures (Concreep 7), France, 2005, pp. 19–38.
[16] Z.P. Bažant, Creep of concrete, in: K.B., et al., (Eds.), Encyclopedia of Materials: Science and Technology, Vol. 2C, Elsevier, Amsterdam, 2001, pp. 1797–1800.
[17] Z. Bažant, A. Hauggaard, S. Baweja, F.-J. Ulm, Microprestress-solidification theory for concrete creep. I. Aging and drying effects, J. Eng. Mech. ASCE 123 (11) (1997) 1188–1194.
[18] B.T. Tamtsia, J.J. Beaudoin, Basic creep of hardened cement paste. A re-examination of the role of water, Cem. Concr. Res. 30 (2000) 1465–1475.
[19] Z. Bažant, Thermodynamics of interacting continua with surfaces and creep analysis of concrete structures, Nucl. Eng. Des. 20 (1972) 477–505.
[20] P. Tennis, H. Jennings, A model for two types of calcium silicate hydrate in the microstructure of Portland cement pastes, Cem. Concr. Res. 30 (2000) 855–863.
[21] Z. Bažant, Creep and Shrinkage in Concrete Structures, J.Wiley & Sons, London, 1982, Chapter 7. Mathematical Models for Creep and Shrinkage of Concrete.
[22] Z. Bažant, Mathematical modeling of creep and shrinkage of concrete, State of the Art in Mathematical Modeling of Creep and Shrinkage of Concrete, J. Wiley, Chichester, 1988.
[23] Z. Bažant, S. Prasannan, Solidification theory for concrete creep: I. Formulation, J. Eng. Mech. 115 (8) (1989) 1691–1703.
[24] M. Jirásek, Z. Bažant, Inelastic Analysis of Structures, John Wiley & Sons, Ltd, 2002.
[25] Z.P. Bažant, Numerically stable algorithm with increasing time steps for integral-type aging creep, in: T. Jaeger (Ed.), Proc. of 1st Int. Conf. on Struct. Mech. in Reactor Tech. (SMiRT-1), 1971, pp. 119–126.
[26] Z. Bažant, Y. Xi, Continuous retardation spectrum for solidification theory of concrete creep, J. Eng. Mech. 121 (2) (1995) 281–288.
[27] Z. Bažant, Criteria for rational prediction of creep and shrinkage of concrete, Revue Française Génie Civil 3 (3–4) (1999) 61–89.
[28] T. Kanit, S. Forest, I. Galliet, V. Mounoury, D. Jeulin, Determination of the size of the representative volume element for random composites: statistical and numerical approach, Int. J. Solids Struct. 40 (2003) 3647–3679.
[29] D.P. Bentz, Quantitative comparison of real and CEMHYD3D model microstructures using correlation functions, Cem. Concr. Res. 36 (2) (2006) 259–263.
[30] V. Šmilauer, Elastic properties of hydrating cement paste determined from hydration models, Ph.D. thesis, ČVUT in Prague, Faculty of Civil Engineering (2006). URL http://cml.fsv.cvut.cz/~smilauer.
[31] H. Moulinec, P. Suquet, A fast numerical method for computing the linear and nonlinear mechanical properties of composites, C. R. Acad. Sci. Ser. II 318 (11) (1994) 1417–1423.
[32] J. Eshelby, The determination of the elastic field of an ellipsoidal inclusion and related problems, Proc. Royal Society of London A, 1957, pp. 376–396.
[33] G. Constantinides, F.-J. Ulm, The effect of two types of C-S-H on the elasticity of cement-based materials: results from nanoindentation and micromechanical modeling, Cem. Concr. Res. 34 (1) (2004) 67–80.
[34] H. Moulinec, P. Suquet, A numerical method for computing the overall response of nonlinear composites with complex microstructure, Comput. Methods Appl. Mech. Eng. 157 (1998) 69–94.
[35] J. Beaudoin, B. Tamtsia, Creep of hardened cement paste — the role of interfacial phenomena, Interface Sci. 12 (2004) 353–360.
[36] J. Beaudoin, B. Tamtsia, Effect of drying methods on microstructural changes in hardened cement paste: an A.C. impedance spectroscopy evaluation, J. Adv. Concr. Technol. 2 (1) (2004) 113–120.
[37] L. Parrot, Recoverable and irrecoverable deformation of heat-cured cement paste, Mag. Concr. Res. 29 (1997) 26–29.
[38] C. Neubauer, H.M. Jennings, E.J. Garboczi, Mapping drying shrinkage deformations in cement-based materials, Cem. Concr. Res. 27 (10) (1997) 1603–1612.
[39] L. Copeland, J. Hayes, The determination of evaporable water in hardened Portland cement paste, ASTM bulletin no. 194, Am. Soc. for Testing Materials, Philadelphia (1953).
[40] Z. Bažant, W. Thonguthai, Pore pressure and drying of concrete at high temperature, J. Eng. Mech. Div. 104 (1978) 1058–1080.
[41] Z. Bažant, M. Kaplan, Concrete at High Temperatures: Material Properties and Mathematical Models, 2nd Edition, Pearson Education, Edinburgh, 2002.
[42] D.P. Bentz, E. Garboczi, C. Haecker, O. Jensen, Effect of cement particle size distribution on performance properties of Portland cement-based materials, Cem. Concr. Res. 29 (1999) 1663–1671.
[43] F. Benboudjema, F. Meftah, J. Torrenti, An unified approach for the modeling of drying shrinkage and basic creep of concrete: analysis of intrinsic behaviour and structural effects, in: N. Bicanic, R.D. Borst, H. Mang, G. Meschke (Eds.), EURO-C Conference on Computational Modelling of Concrete Structures, 2003, pp. 391–400.
[44] O. Bernard, F.-J. Ulm, T. Germaine, Volume and deviator creep of calcium-leached cement-based materials, Cem. Concr. Res. 33 (8) (2003) 1127–1136.
[45] H. Stehfest, Algorithm 368, numerical inversion of Laplace transforms, Commun. ACM 43 (1) (1970) 47–49.
[46] F. Bell, A survey of the engineering properties of some anhydrite and gypsum from the north and midlands of England, Eng. Geol. 38 (1–2) (1994) 1–23.
[47] S. Kamali, M. Moranville, E. Garboczi, S. Prené, B. Gérard, Hydrate dissolution influence on the young's modulus of cement paste, in: L., et al., (Eds.), Proc. Fracture Mechanics of Concrete Structures (FraMCoS-V), Routledge, Vail, 2004, pp. 631–638.